Article

Characteristics of Natural Ti-Bearing Nanoparticles in Groundwater within Karst Areas of Northern China

Lei Zuo [1], Changsuo Li [2,*], Peng Zhang [1], Yaqin Wang [1], Shuai Gao [2], Bin Sun [2] and Rui Liu [1,*]

[1] School of Resources and Environmental Engineering, Shandong University of Technology, Zibo 255000, China; zoey.6521@outlook.com (L.Z.); 18111006060@stumail.sdut.edu.cn (P.Z.); 19121006067@stumail.sdut.edu.cn (Y.W.)

[2] 801 Institute of Hydrogeology and Engineering Geology, Shandong Provincial Bureau of Geology and Mineral Resources, Jinan 250014, China; shuaigao90@126.com (S.G.); spinhlr@163.com (B.S.)

* Correspondence: lics120@163.com (C.L.); liurui@sdut.edu.cn (R.L.)

Abstract: Karst areas are widespread in China and can be divided into southern karst and northern karst based on the geographical boundary of Qinling Mountains and Huaihe River. In northern karst regions, karst springs are the predominant landform. Previous studies on karst springs have predominantly focused on macroscopic perspectives, such as water chemistry characteristics, with less attention given to the microscopic characteristics of springs. Therefore, this study focused on the Jinan Baotu Spring area, representative of a typical northern karst region, and investigated the natural nanoparticles present in different aquifers at various depths from a microscopic point of view. Through the observation of nanoparticle tracking analyzer (NTA), numerous nanoparticles were identified in the groundwater samples. The particle size range of the particles contained in groundwater is mainly concentrated in the range of 150–500 nm, and the particle concentration is mainly concentrated in the range of $1.5–5.0 \times 10^5$ Particles/L. The microstructure, chemical composition, and element distribution of these nanoparticles were analyzed using TEM-EDS techniques. The results unveiled the presence of Ti-bearing nanoparticles in various groundwater layers, including both crystalline and amorphous states, as well as nanoparticles exhibiting the coexistence of crystal and amorphous structures. By comparing the measured lattice spacing with PDF cards, the crystalline Ti-bearing nanoparticles were identified as rutile, brookite, anatase, ilmenite, pseudorutile, and ulvospinel. Furthermore, the main components of the amorphous Ti-bearing nanoparticles predominantly consisted of Ti or a mixture of Ti and Fe. EDS analysis further indicated that the Ti-bearing nanoparticles carried additional metal elements, such as Zn, Ca, Mn, Mo, Cr, and Ni, suggesting their potential role as carriers of metal elements during groundwater transportation. This discovery provided new insights into the migration of metal elements in groundwater and underscores the capacity of nanoparticles to enhance the mobility of inorganic substances within the water environment. Notably, brookite was detected in three different areas, including the direct discharge area, indirect recharge area, and discharge area, which may indicate that some special natural nanoparticles could serve as natural mineral tracer particles in the process of groundwater migration.

Keywords: Jinan Baotu Spring area; groundwater; nanoparticles; Ti; carrier; tracer particles

1. Introduction

Numerous investigations have shown the presence of a significant quantity of natural nanoparticles in groundwater [1–4]. These nanoparticles originate from both geochemical and biological processes. Owing to their distinctive physicochemical properties, nanoparticles can provide valuable insights into their environment [1,5,6]. Moreover, they have the ability to persist over extended periods and facilitate the transportation of elements [7,8]. Microscopic observation of daily drinking water revealed the existence of irregularly shaped nanoscale and microscopic solid materials [9]. Similarly, Faulstich et al. [10] identified microscopic nanoparticles in natural mineral water and nearby sediments in Aachen,

Germany. Currently, engineered nanoparticles (ENPs), such as TiO_2 [11], zero-valent iron (nZVI) [12,13], iron oxide nanoparticles [14,15], and titanium (Ti) iron oxide [16], are frequently employed as cost-effective adsorbents for arsenic (As) removal from water. Despite the release of these ENPs into the environment, they constitute only a minor portion of the overall nanoparticle content [3]. Furthermore, although ENPs can enhance water quality, they also pose environmental hazards. Consequently, considering that drinking water serves as a significant pathway for nanoparticle exposure, the lack of studies on natural nanoparticles in groundwater necessitates further investigation and a thorough examination of their microscopic characteristics and origins. Such endeavors are crucial for a comprehensive understanding of the significant role played by natural nanoparticles in groundwater circulation and transportation.

Karst areas in China are extensively distributed, accounting for about 1/3 of the national territory, which positions China at the forefront globally [17,18]. Karst aquifers not only have the potential to be significant water resources but are also recognized for being dominated by subsurface systems that are challenging to characterize [19]. With the Qinling Mountains and Huaihe River as the boundary, these regions can be divided into southern and northern karst areas, with noticeable disparities in their development. In the northern regions, karst formations primarily manifest as karst springs, with the renowned Baotu spring in Jinan serving as a representative example. Spring water originates from the upward movement of karst groundwater, emerging vertically onto the surface [20]. Jinan Baotu Spring holds historical significance as a vital source of drinking water and landscape water in Jinan [21]. However, the interplay of natural and anthropogenic factors has altered groundwater recharge, runoff, and discharge dynamics, disrupting the natural equilibrium of karst water systems and undermining the natural chemical balance of groundwater. Consequently, the disappearance of spring water has become an imminent threat [22–25]. The aquifer medium in the Baotu Spring area of Jinan exhibits complex and diverse characteristics, necessitating the exploration of innovative research methods for groundwater analysis. This study delved into an examination of natural Ti-bearing nanoparticles in groundwater, including their ultrastructure (morphology, size, crystal form, crystalline state, and polymerization state), chemical composition, and element distribution across different groundwater layers. The findings illuminate the distinct attributes of Ti-bearing nanoparticles in each layer, thereby offering new insights into the groundwater circulation system.

2. Geological Setting

Jinan is located in the central region of Shandong Province, China (Figure 1a). It is bordered by Mount Tai to the south, the Yellow River to the north, Liaocheng to the west, and Zibo to the east. The Baotu Spring area is positioned in the north-central area of Jinan, characterized by a topographical variation where the southeastern part features higher elevations, while the northwestern part exhibits lower elevations. The southern region comprises mountainous terrain, whereas the northern area consists of a piedmont clinoplain. Notably, the absolute elevation gradually decreases from 500–600 m in the south to 25–50 m in the north.

The study area is located at the junction of the northern periphery of the central Shandong mountain range and the piedmont clinoplain. The terrain exhibits a south-to-north and east-to-west gradient, characterized by higher elevations in the south and east, and lower elevations in the north and west. The overall geological structure is characterized by a monocline formation, where the southern region consists of an expansive, undulating mountainous area with the prominent Mount Tai ridge traversing in an east–west direction, featuring steep slopes. In contrast, the northern part encompasses an alluvial plain. The study area is situated in the northern wing of Mount Tai vault. It exhibits a geological structure characterized by a northward inclined monocline formation, which is predominantly composed of Paleozoic strata. The primary structural type in the area is brittle rupture.
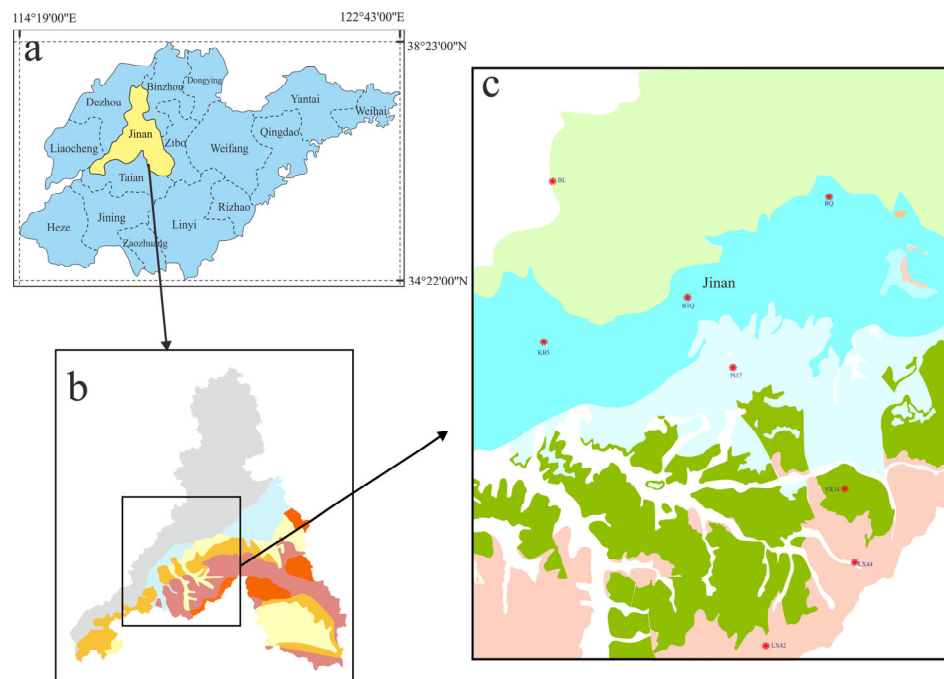
Figure 1. Geographical location of Jinan and the locations of the sampling points ((**a**): Location map of Jinan City; (**b**): Sample collection area; (**c**): Sampling point location map).

The exposed strata in the study area, from south to north, include the Archean Taishan Group (Art), Paleozoic Cambrian ($\in$), Ordovician (O), Carboniferous–Permian (C-P), and Cenozoic Quaternary (Q) formations. The Archean Taishan Group is distributed in the southern watershed area of Jinan and encompasses lithology such as biotite dioritic gneiss, amphibolite, amphibole plagioclase gneiss, and biotite granulite, constituting the basal layer of the area. The Cambrian formation is mostly distributed in the south-central part of Jinan and primarily consists of shale and limestone. The Ordovician formation is located in the north-central part of Jinan and comprises mainly shale and limestone. The Carboniferous–Permian formation is distributed north of Jinan and is mainly composed of shale, conglomerate, and sandstone. Lastly, the Cenozoic Quaternary formation is widely distributed throughout the alluvial plains formed by river valleys, submontane rivers, and along the Yellow River, mainly characterized by silty clay and silt.

The Jinan Baotu Spring area is located in a mid-latitude inland area, characterized by a warm temperate continental monsoon climate, exhibiting distinct seasonal variations and significant winds. The annual average temperature is 14.3 °C, the average precipitation is 646.6 mm, and the annual average evaporation ranges between 1500 mm and 1900 mm (data from 2021–2023). Precipitation distribution throughout the year is uneven, with the flood season occurring from June to September, accounting for approximately 73% of the annual precipitation. Evaporation displays substantial variation across different seasons, with the highest rates observed during the spring and summer months of April to July, contributing to more than 53% of the annual evaporation. In contrast, the winter months of December to February experience the lowest evaporation rates, amounting to less than 10% of the annual evaporation. Considering the lithological composition of aquifer medium and the formation and enrichment characteristics of groundwater, the groundwater aquifer group in Jinan can be primarily categorized into four types: loose rock pore space aquifers, carbonate fracture karst aquifers, clastic rock sandwiched with carbonate karst fracture aquifers, and magma rock and metamorphic rock fractured aquifers (Figure 2).
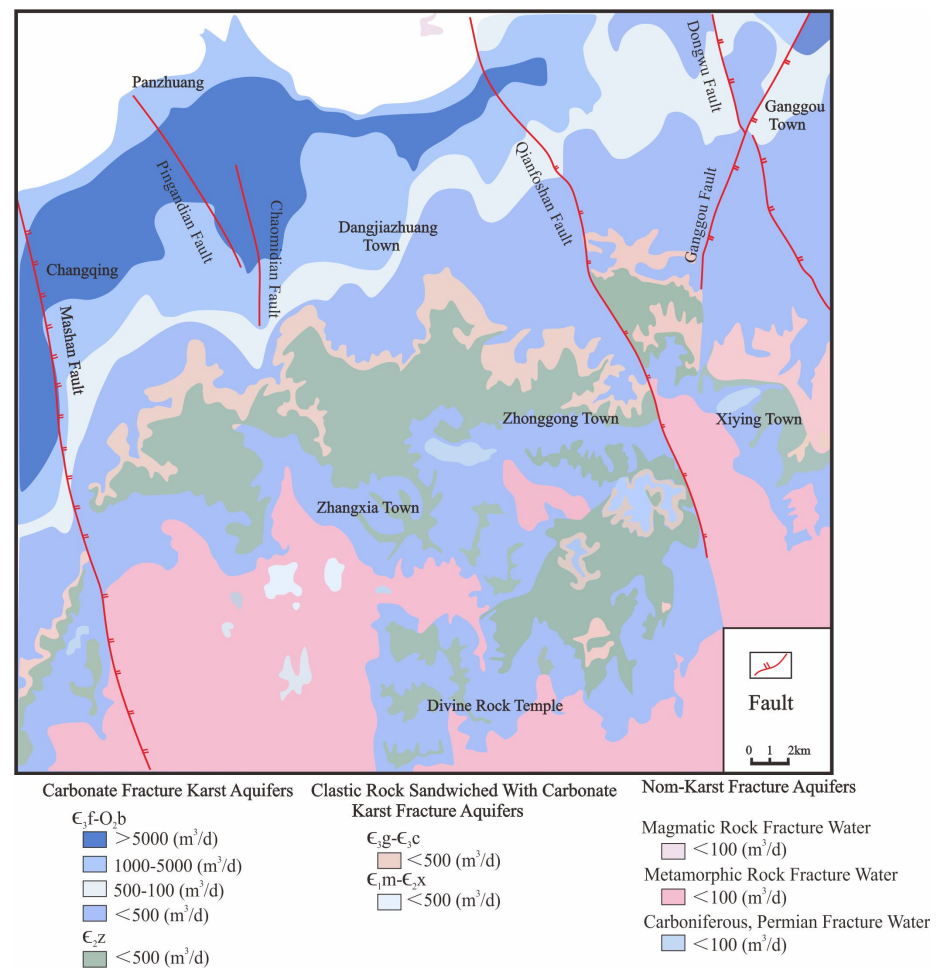
Figure 2. Hydrogeological map of Baotu Spring Area.

Loose rock pore space aquifers are predominantly distributed in the northern Yellow River alluvial plain and mountainous river valley areas. The eastern and western suburban porous aquifers have hydraulic connectivity in certain local sections with karst aquifers, forming a complementary relationship. Atmospheric precipitation infiltration is the primary source of recharge, and the predominant direction of groundwater movement is from south to north, with agricultural irrigation being the main discharge method. The carbonate fracture karst aquifers are primarily composed of Cambrian–Ordovician aquifers, which can be further divided into the Chaomidian formation to the Majiagou formation, forming a continuous and thick fractured karst aquifer rock group, along with the separate Zhangxia formation fractured karst aquifer rock group. The clastic rock sandwiched with carbonate karst fracture aquifers consists of limestones from the Cambrian Mantou formation, Xuzhuang formation, and Changshan formation. Due to the interlayering of limestones and shales in this aquifer, fractures are not well developed, resulting in poor aquifer productivity. The magma rock and metamorphic rock fractured aquifers have extremely poor and uneven aquifer productivity. Groundwater occurrence and movement mainly take place in the pores and fractures of rocks within weathered zones of granite gneiss, slate, gabbro, and diorite, with the groundwater flow direction being largely controlled by the terrain slope.

Cambrian–Ordovician limestone is widely distributed in the South Mountain area of Jinan, exhibiting well-development karst features both on the surface and underground. The main source of karst water in Jinan is direct infiltration replenishment from atmospheric precipitation. In general, rivers experience surface flow during the rainy season, facilitating the leakage recharge of river water into karst water, whereas in the dry season, the rivers

cease to flow, resulting in the formation of dry valleys. Therefore, atmospheric precipitation recharge and surface water leakage recharge serve as the primary sources of karst water replenishment in Jinan spring area. The runoff direction of karst water in Jinan spring area generally aligns with the inclination direction of terrain and rock strata, predominantly flowing from south to north. The numerous large and small springs scattered across Jinan serve as natural discharge points of the karst groundwater. However, the increasing demands of urban, industrial, and agricultural activities have led to escalating groundwater exploitation in the Jinan area. Consequently, the flow of the four major spring groups in Jinan has been progressively declining, with complete cessation during the dry season. Therefore, artificial mining and spring water discharge have become the main mechanisms for the discharge of karst water in Jinan.

3. Sampling and Analytical Methods

3.1. Sampling Sites

This study focused on investigating the Baotu Spring area of Jinan City as the primary research area, from which a total of 8 groundwater samples were collected across different locations. To ensure accurate sampling, a volumetric flask with a capacity of 50 mL was employed. Each sample was collected by first rinsing the flask, followed by filling it with more than 30 mL of groundwater. The flask was then tightly sealed and securely stored. The collected samples consisted of 2 groundwater samples from spring water, 5 from central karst water, and 1 from deep geothermal water. The specific locations of the sampling points are shown in Figure 1b,c.

3.2. Analytical Methods

Firstly, the particle size and concentration of the groundwater samples were determined using nanoparticle tracking analysis (NTA) at the laboratory with ZetaView PMX 110 (Particle Metrix, Meerbusch, Germany) and corresponding software ZetaView 8.04.02. The NTA measurements were recorded and analyzed at 11 different positions. To ensure accurate measurements, the ZetaView system was calibrated using 110 nm polystyrene particles while maintaining the temperature within the range of around 23 °C to 30 °C.

For the test analysis in this study, nanoparticle transmission electron microscopy (TEM) was primarily adopted. The maximum acceleration voltage for TEM was 200 kV. TEM foils were prepared by extracting and attaching them to Cu grids via Pt welding, followed by thinning them to thicknesses of 50–70 nm. High-angle annular dark-field scanning transmission electron microscopy (HAADF-STEM) imaging was performed using an ultra-high-resolution and probe-corrected FEI Titan Themis TEM. The processing of high-resolution transmission electron microscopy (HRTEM) images, including fast Fourier transform (FFT), was conducted using Gatan's Digital Micrograph software (version 3.7.4). Moreover, the elemental distribution was determined by energy-dispersive X-ray spectrometry (EDS). All analyses, including TEM and EDS, took place at the Sinoma Institute of Materials Research (Guangzhou, China) Co., Ltd.

4. Results

Firstly, according to the experimental data results obtained from the NTA test (Table 1), it was evident that numerous nanoparticles were present in the groundwater samples collected from different layers. The particle size of these particles in different types of groundwater mainly fell with the range of 150–500 nm, and the particle concentration typically ranged from 1.5 to 5.0 $\times$ 10^5 Particles/L. Notably, the particle size ranges of nanoparticles in the samples collected from spring water and deep geothermal water were basically the same. However, there was considerable variation in the particle size ranges of nanoparticles found in different samples collected from karst water, indicating a potential correlation with environmental instability.

Table 1. Basic information on samples.

Samples	Size (nm)	Concentration (Particles/mL)	Groundwater Types	Area
BQ	155.9–352.0	$2.5\text{–}4.1 \times 10^5$	Spring	Discharge area
BTQ	151.5–355.6	$0.95\text{–}1.9 \times 10^5$		
LX42	149.3–410.6	$5.8\text{–}6.9 \times 10^4$	Karst water	Indirect recharge area
LX44	152.9–408.6	$0.82\text{–}1.8 \times 10^5$		Indirect recharge area
JS12	183.1–299.4	$1.2\text{–}1.5 \times 10^6$		Direct recharge area
KB5	155.0–418.5	$1.6\text{–}5.3 \times 10^5$		Discharge area
YR34	194.8–513.2	$3.7\text{–}8.1 \times 10^4$		Indirect recharge area
BL	152.6–469.5	$1.6\text{–}3.9 \times 10^5$	Geothermal water	Northern geothermal heat

Through the analysis of TEM images and EDS energy spectrum of nanoparticles in groundwater, it was observed that 19 nanoparticles containing Ti were present in the collected groundwater samples. These Ti-bearing particles originated from groundwater at different levels, as confirmed by spot analysis using EDS (Table 2). Since the grid of TEM is made of Cu with a carbon (C) film, these Ti-bearing nanoparticles exhibited higher contents of C and Cu, which aligned with the uniform distribution of C and Cu observed in the EDS map.

Table 2. EDS results of sample particles.

Sample	N	O	Ti	Mg	Al	Si	S	K	Ca	Mn	Fe	V	P	Zn	Ar	Cr	Co	Mo	Ni	Cl	Zr
BQ-1	-	61.84	34.11	-	1.16	1.13	0.52	-	0.58	-	0.66	-	-	-	-	-	-	-	-	-	-
BTQ-1	-	50.44	49.56	-	-	-	-	-	-	-	-	-	-	-	-	-	-	-	-	-	-
BTQ-2	17.07	43.47	39.45	-	-	-	-	-	-	-	-	-	-	-	-	-	-	-	-	-	-
BQT-3	12.06	51.64	36.31	-	-	-	-	-	-	-	-	-	-	-	-	-	-	-	-	-	-
BTQ-4	11.53	47.67	40.79	-	-	-	-	-	-	-	-	-	-	-	-	-	-	-	-	-	-
LX42-1	18.16	42.17	31.20	-	0.65	1.38	-	-	-	-	-	-	-	-	-	-	1.80	-	1.34	-	3.32
LX44-1	17.01	47.08	35.91	-	-	-	-	-	-	-	-	-	-	-	-	-	-	-	-	-	-
LX44-2	18.51	49.10	31.03	-	0.43	0.94	-	-	-	-	-	-	-	-	-	-	-	-	-	-	-
JS12-1	14.60	53.85	7.00	0.89	3.94	4.27	0.53	1.12	1.83	0.86	11.09	-	-	-	-	-	-	-	-	-	-
JS12-2	6.87	43.57	20.98	-	1.68	2.16	-	-	1.06	-	23.67	-	-	-	-	-	-	-	-	-	-
JS12-3	12.87	38.89	39.01	-	0.42	0.38	-	-	-	-	2.95	5.48	-	-	-	-	-	-	-	-	-
JS12-4	16.09	39.73	39.87	-	2.37	0.10	0.39	-	1.12	-	-	-	0.33	-	-	-	-	-	-	-	-
JS12-5	16.37	44.60	38.28	-	0.52	0.24	-	-	-	-	-	-	-	-	-	-	-	-	-	-	-
JS12-6	11.99	48.22	34.67	-	1.75	0.80	0.24	-	0.48	-	-	-	-	1.85	-	-	-	-	-	-	-
KB5-1	-	50.32	6.12	-	3.89	0.87	-	-	-	1.41	5.24	0.94	-	-	2.77	8.12	8.37	2.56	9.38	-	-
KB5-2	-	52.47	13.55	0.79	6.64	1.13	6.10	-	-	1.87	3.96	2.08	-	-	4.38	1.60	-	3.83	1.59	-	-
YR34-1	14.93	29.20	32.41	1.80	0.99	3.24	0.96	0.23	3.32	-	-	-	0.39	-	-	-	-	-	-	12.53	-
BL-1	-	37.13	5.59	-	0.95	1.83	-	-	2.01	-	52.50	-	-	-	-	-	-	-	-	-	-
BL-2	-	33.42	5.77	-	0.69	1.40	-	-	1.23	-	56.81	-	0.69	-	-	-	-	-	-	-	-

4.1. Characteristics of Natural Nanoparticles in Spring Water

The Ti particles found in the spring water samples mainly existed in the form of Ti oxides. Specifically, the Ti-bearing nanoparticles in the Baotu Spring exhibited a relatively simple composition, consisting of only nitrogen (N), oxygen (O), and Ti elements. The Ti content in these particles was generally higher compared to the deep geothermal water samples. Figure 3 illustrates the presence of irregular Ti-bearing nanoparticles in samples collected from Baiquan (BQ) and Baotu Spring (BTQ).
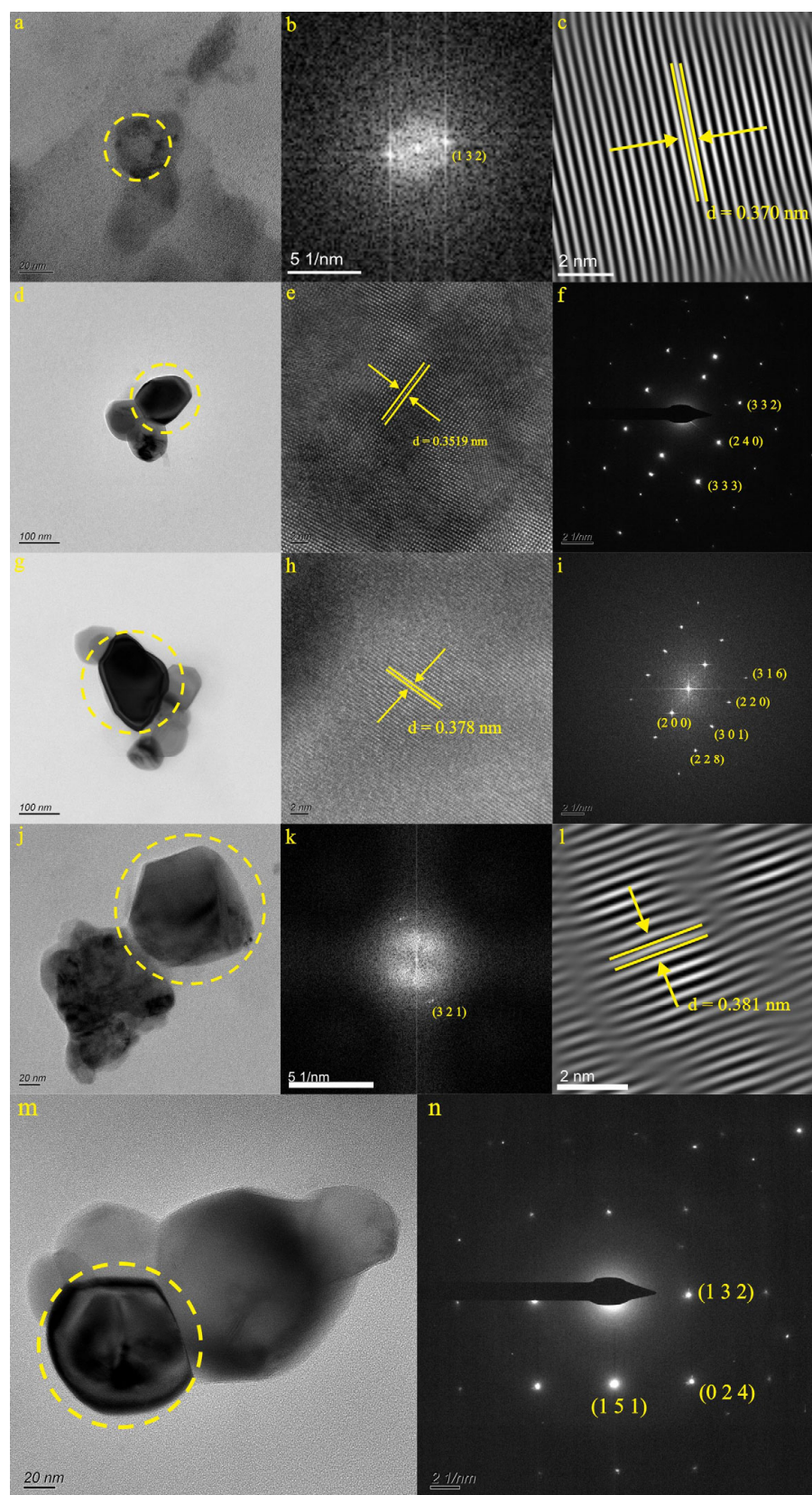
Figure 3. Particle morphology, high-resolution image, diffraction pattern and Lattice spacing of BQ and BTQ samples ((**a**,**d**,**g**,**j**,**m**): particle morphology; (**e**,**h**): high-resolution image; (**b**,**f**,**i**,**k**,**n**): diffraction pattern; (**c**,**l**): lattice spacing).

There was only one Ti-bearing nanoparticle present in the Baiquan (BQ) sample. Figure 3a depicts the particle from the BQ-1 sample, while the selected area electron diffraction (SAED) pattern of the specific area (indicated by the dotted circle) in Figure 3b revealed a relatively well-ordered structure of the Ti-bearing nanoparticle. The measured d-spacing was clearly observed to be 3.70 Å (1 3 2) (Figure 3c). EDS analysis determined that the particle mainly contained O (61.84%) and Ti (34.11%). The composition of the particle corresponded to the data found in PDF card 29-1360, leading to the identification of the particle in Figure 3a as brookite (TiO_2).

The Baotu Spring (BTQ) sample contained four Ti-bearing nanoparticles (Figure 3d,g,j,m). Figure 3d presents the BTQ-1 sample particle, where the high-resolution image reveals neatly arranged crystal planes, with the d-spacing clearly measured as 3.517 Å (Figure 3e). The SAED pattern of the specific area (indicated by the dotted circle) in Figure 3f demonstrates a relatively well-ordered structure of the Ti-bearing nanoparticle, with the d-spacing clearly measured as 3.511 Å (1 2 0), 2.318 Å (0 4 0), 3.517 Å (1 2 0), 1.333 Å (3 3 2), and 1.685 Å (3 2 0) (Figure 3f). EDS analysis determined that the particle mainly contained O (50.44%) and Ti (49.56%). The composition of the particle aligns with the data found in PDF card 29-1360, leading to the identification of the particle in Figure 3d as brookite (TiO_2). Figure 3g depicts the BTQ-2 sample particle, revealing clearly neatly arranged crystal planes in the high-resolution image, with the d-spacing clearly measured as 3.78 Å (Figure 3h). The SAED pattern of the specific area (indicated by the dotted circle) in Figure 3i shows a relatively well-ordered structure of the Ti-bearing nanoparticle, with the d-spacing clearly measured as 3.780 Å (2 0 0), 1.782 Å (2 2 8), 2.490 Å (3 0 1), 2.612 Å (2 2 0), and 1.904 Å (3 1 6) (Figure 3i). Through EDS analysis, it was determined that the particle mainly contained N (17.07%), O (43.47%), and Ti (39.45%). The composition of the particles aligned with the data found in PDF card 21-1272, resulting in the identification of the particle in Figure 3g as anatase (TiO_2). Figure 3j illustrates the BTQ-3 sample particle. The SAED pattern of the specific area (indicated by the dotted circle) in Figure 3k reveals a relatively well-ordered structure of the Ti-bearing nanoparticle, with the d-spacing clearly measured as 3.81 Å (3 2 0) (Figure 3l). EDS analysis determined that the particle primarily consisted of N (12.06%), O (51.64%), and Ti (36.31%). The composition of the particles matched the data found in PDF card 21-1276, leading to the identification of the particle in Figure 3j as rutile (TiO_2). Figure 3m represents the BTQ-4 sample particle, while the SAED pattern of the specific area (indicated by the dotted circle) in Figure 3n demonstrates a relatively well-ordered structure of the Ti-bearing nanoparticle. The measured d-spacing is clearly observed to be 1.646 Å (1 5 1), 1.240 Å (0 2 4), and 1.866 Å (1 3 2) (Figure 3n). Through EDS analysis, it was determined that the particle primarily consisted of N (11.53%), O (47.67%), and Ti (40.79%). The composition of the particle matched the data found in PDF card 29-1360, resulting in the identification of the particle in Figure 3m as brookite (TiO_2).

4.2. Characteristics of Natural Nanoparticles in Karst Water

The Ti particles in the karst water samples mainly existed in the form of Ti oxides, with a higher Ti content compared to deep geothermal water samples. Figures 4–6 display irregular Ti-bearing nanoparticles found in samples from LX42, LX44, JS12, KB5, and YR34.

4.2.1. Characteristics of Natural Ti-Bearing Nanoparticles in LX42 and LX44 Samples

Within the LX42 sample, only one Ti-bearing nanoparticle was identified. Figure 4a illustrates the LX42-1 sample particle. The SAED pattern within the domain (indicated by the dotted circle) (Figure 4b) reveals a relatively well-ordered structure of the Ti-bearing nanoparticle, with the d-spacing clearly measured as 3.70 Å (1 3 2) (Figure 4c). EDS analysis determined that the particle primarily contained N (18.16%), O (42.17%), and Ti (31.20%). The composition of the particle matched the data found in PDF card 29-1360, leading to the identification of the particle in Figure 4a as brookite (TiO_2).

Two Ti-bearing nanoparticles were identified in the LX44 sample (Figure 4d,f). Figure 4d shows the LX44-1 sample particle, and the SAED pattern within the domain (indicated

by the dotted circle) (Figure 4e) demonstrates a relatively well-ordered structure of the Ti-bearing nanoparticle, with the d-spacing clearly measured as 1.761 Å (2 4 0), 1.66 Å (2 4 1), 1.21 Å (4 3 1), and 2.231 Å (0 4 0) (Figure 4e). Based on EDS analysis, it was determined that the particle mainly contained N (17.01%), O (47.08%), and Ti (35.91%). The composition of the particle aligned with the data found in PDF card 29-1360, leading to the identification of the particle in Figure 4d as brookite (TiO_2). Figure 4f presents the LX44-2 sample particle. The SAED pattern within the domain (indicated by the dotted circle) (Figure 4g) reveals a relatively well-ordered structure of the Ti-bearing nanoparticle, with the d-spacing clearly measured as 2.389 Å (1 2 4), 1.613 Å (1 1 3), and 3.106 Å (1 2 3) (Figure 4g). EDS analysis determined that the particle mainly contained N (18.51%), O (49.10%), and Ti (31.03%). The composition of the particle matched the data found in PDF card 29-1360. Hence, the particle in Figure 4f was identified as brookite (TiO_2).
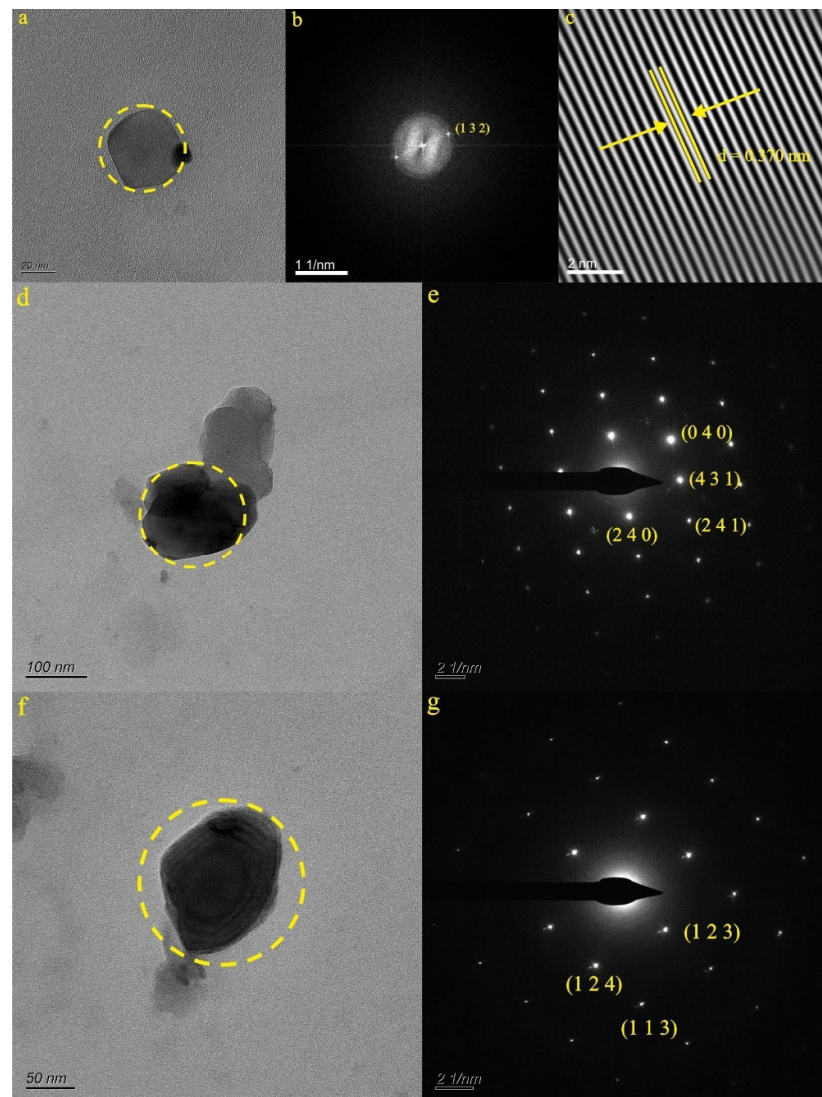

Figure 4. Particle morphology, diffraction pattern, and lattice spacing of LX42 and LX44 samples ((**a**,**d**,**f**): particle morphology; (**b**,**e**,**g**): diffraction pattern; (**c**): lattice spacing).
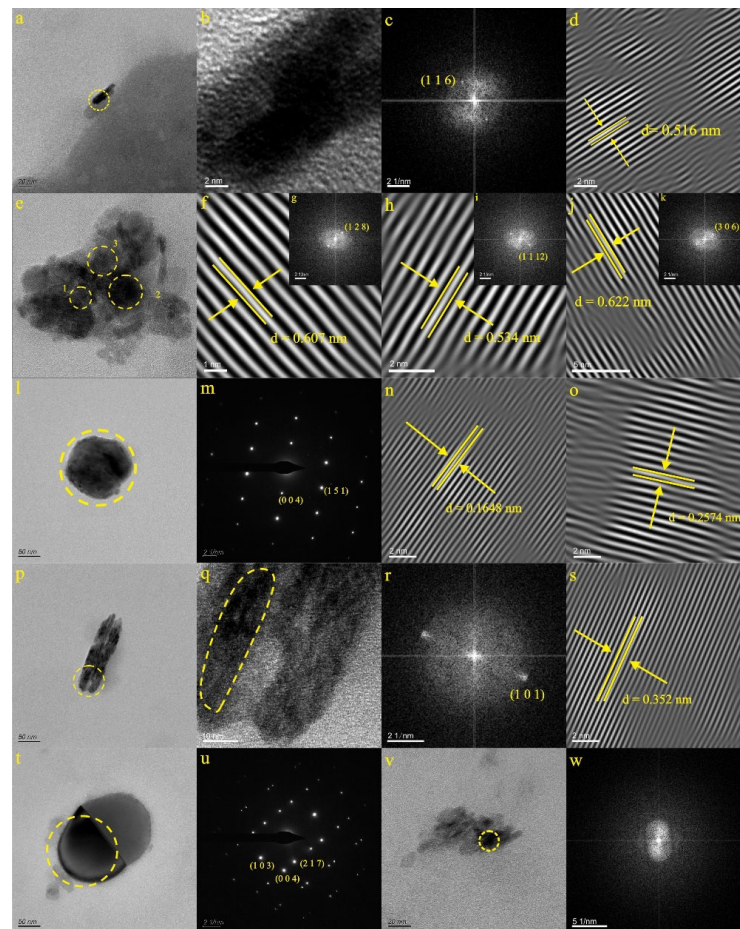
Figure 5. Particle morphology, high-resolution image, diffraction pattern, and lattice spacing of JS12 samples ((**a**,**e**,**l**,**p**,**t**,**v**): particle morphology; (**b**,**q**): high-resolution image; (**c**,**g**,**i**,**k**,**m**,**r**,**u**,**w**): diffraction pattern; (**d**,**f**,**h**,**j**,**n**,**o**,**s**): lattice spacing).
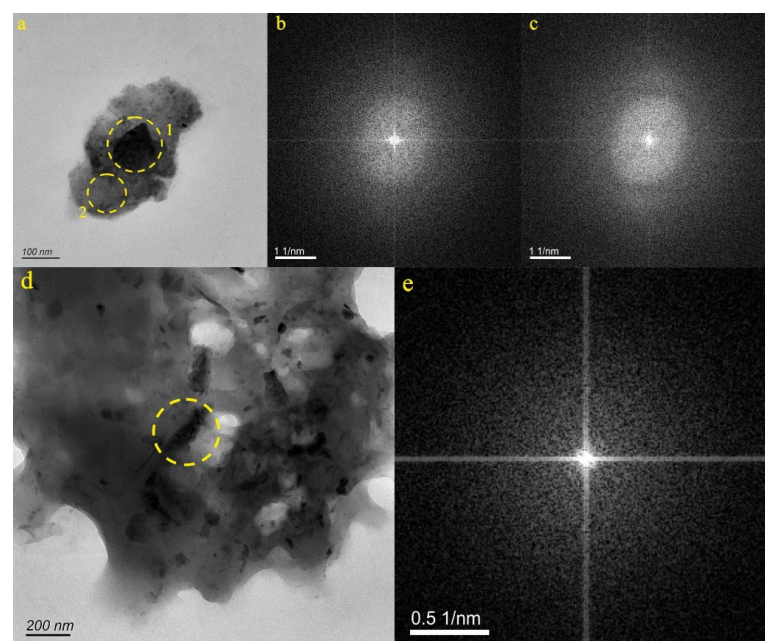
Figure 6. Particle morphology and diffraction pattern of KB5 and YR34 samples ((**a**,**d**): particle morphology; (**b**,**c**,**e**): diffraction pattern).

4.2.2. Characteristics of Natural Ti-Bearing Nanoparticles in JS12 Sample

In the JS12 sample, a total of six Ti-bearing nanoparticles were identified (Figure 5a,e,l,p,t,v). Figure 5a presents the JS12-1 sample particle, where the high-resolution image (Figure 5b) reveals partially arranged crystal planes. The SAED pattern within the domain (indicated by the dotted circle) (Figure 5c) demonstrates a relatively well-ordered structure of the Ti-bearing nanoparticle, with the measured d-spacing clearly being 5.16 Å (1 1 6) (Figure 5d). The EDS analysis determined that the particle mainly consisted of N (14.60%), O (53.85%), Ti (7.00%), Al (3.94%), Si (4.27%), and Fe (11.09%). The composition matched the data found in PDF card 29-0733, thus identifying the particle in Figure 5a as ilmenite ($Fe^{2+}TiO_3$). Figure 5e displays the JS12-2 sample particle, presenting three different sets of lattice spacing. The SAED pattern with the domain (indicated by the dotted circle) (Figure 5g,i,k) reflects a relatively well-ordered structure of the Ti-bearing nanoparticle, with the d-spacing clearly measured as 6.07 Å (1 2 8) (Figure 5f), 5.34 Å (1 1 12) (Figure 5h), and 6.22 Å (3 0 6) (Figure 5j). The EDS analysis indicated that the particle mainly contained N (6.87%), O (43.57%), Ti (20.98%), and Fe (23.67%). The composition matched the data found in PDF card 29-0733; Therefore, the particle in Figure 5e was identified as ilmenite ($Fe^{2+}TiO_3$). Figure 5l depicts the JS12-3 sample particle. The SAED pattern within the domain (indicated by the dotted circle) (Figure 5m) reveals a relatively well-ordered structure of the Ti-bearing nanoparticle, with the d-spacing clearly measured as 1.648 Å (1 5 1) and 2.574 Å (0 0 4) (Figure 5n,o). The EDS analysis determined that the particle mainly contained N (12.87%), O (38.89%), Ti (39.01%), V (5.48%), and Fe (2.95%). The composition matched the data found in PDF card 29-1360, thereby identifying the particle in Figure 5l as brookite (TiO_2). Figure 5p depicts the JS12-4 sample particle, revealing partially arranged crystal planes in the high-resolution image (Figure 5q). The SAED pattern within the domain (dotted circle) (Figure 5r) displays a relatively well-ordered structure of the Ti-bearing nanoparticle, with the d-spacing clearly measured as 3.52 Å (1 0 1) (Figure 5s). The EDS analysis determined that the particle mainly contained N (16.09%), O (39.73%), and Ti (39.87%). The composition matched the data found in PDF card 21-1272. Consequently, the particle in Figure 5p was identified as anatase (TiO_2). Figure 5t shows the JS12-5 sample particle, and the selected area electron diffraction (SAED) pattern of the domain (indicated by the dotted circle) (Figure 5u) presents a relatively well-ordered structure of the Ti-bearing nanoparticle, with the d-spacing clearly measured as 2.428 Å (1 0 3), 2.380 Å (0 0 4), and 3.182 Å (2 1 7) (Figure 5u). The EDS analysis determined that the particle mainly contained N (16.37%), O (44.60%), and Ti (38.28%). The composition matched the data found in PDF card 21-1272, thus identifying the particle in Figure 5t as anatase (TiO_2). Figure 5v presents the JS12-6 sample particle, and the SAED pattern with the domain (dotted circle) (Figure 5w) indicates that the Ti-bearing nanoparticle was amorphous. Through the EDS analysis, it was determined that the particle mainly contained N (16.37%), O (44.60%), and Ti (38.28%). Thus, the particle in Figure 5v mainly represented a Ti-bearing nanoparticle.

4.2.3. Characteristics of Natural Ti-Bearing Nanoparticles in KB5 and YR34 Samples

The KB5 sample contained two Ti-bearing nanoparticles (Figure 6a). Figure 6a illustrates the presence of these nanoparticles, and the SAED pattern with the respective domains (dotted circles) (Figure 6b,c) reveals their amorphous nature. The EDS analysis unveiled that particle 1 mainly contained O (50.32%), Ti (6.12%), Co (8.37%), Cr (8.12%), Fe (5.24%), and Ni (9.38%), while particle 2 primarily consisted of O (52.47%), Ti (13.55%), Al (6.64%), S (6.10%), Fe (3.96%), Ar (4.38%), and Mo (3.83%). Consequently, the particles depicted in Figure 6a may represent polymetallic oxides.

In the YR34 sample, there existed only one Ti-bearing nanoparticle. Figure 6d presents the YR34 sample particle, and the SAED pattern with the domain (dotted circle) (Figure 6e) indicates that the Ti-bearing nanoparticle was amorphous. EDS analysis determined that the particle mainly contained N (14.93%), O (29.20%), Ti (32.41%), and Cl (12.53%). Thus, the particle in Figure 6d mainly represents a Ti-bearing nanoparticle.

4.3. Characteristics of Natural Nanoparticles in Deep Geothermal Water

There were two Ti-bearing nanoparticles in the Beilin (BL) sample (Figure 7). Figure 7a displays the BL-1 sample particle, and the SAED pattern within the domain (dotted circle) (Figure 7b) reveals that the Ti-bearing nanoparticle exhibited an amorphous structure. The EDS analysis determined that the particle mainly contained O (37.13%), Fe (52.50%), and Ti (5.59%), suggesting that the nanoparticle mainly contained Ti and Fe, as depicted in Figure 7a. Figure 7c illustrates the BL-2 sample particle, displaying two different sets of lattice spacing in the high-resolution image (Figure 7d). The SAED pattern within the domains (dotted circles) (Figure 7f,h) reveals a relatively well-ordered structure of the Ti-bearing nanoparticle, with the d-spacing clearly measured as 1.81 Å (7 5 1) (Figure 7e) and 1.97 Å (6 6 4) (Figure 7g). The EDS analysis determined that the particle mainly contained O (33.42%), Fe (56.81%), and Ti (5.77%), aligning with the data from PDF card 34-0177. Therefore, the particle depicted in Figure 7c was identified as ulvospinel (Fe_2TiO_4).
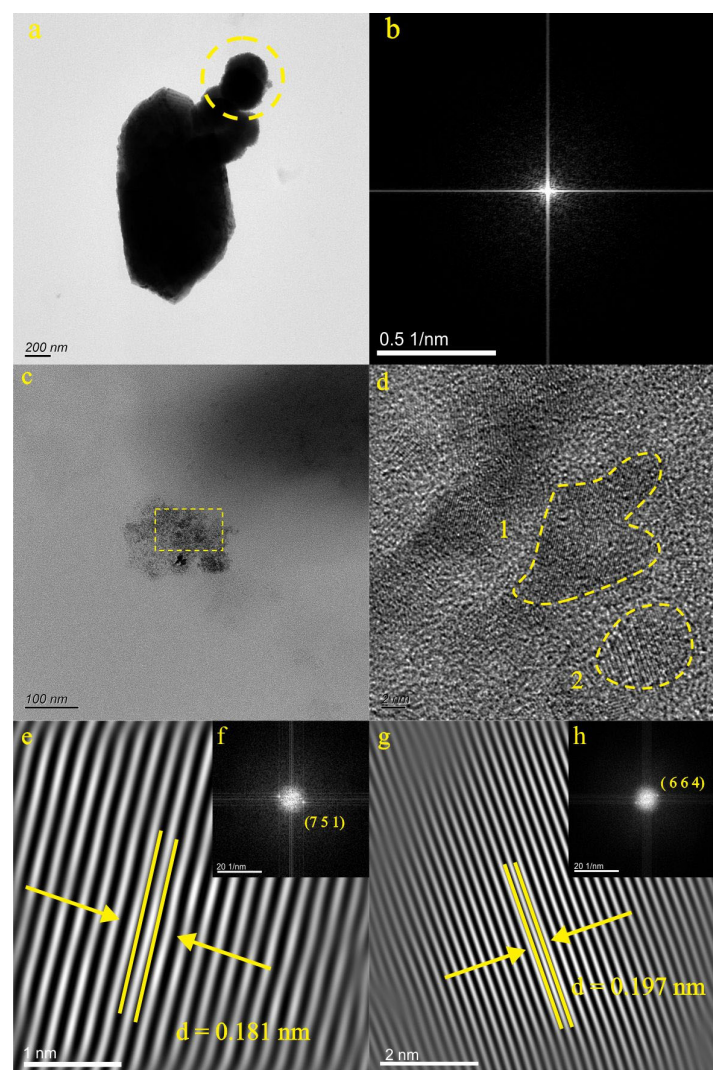

Figure 7. Particle morphology, high-resolution image, diffraction pattern, and lattice spacing of BL samples ((**a**,**c**): particle morphology; (**d**): high-resolution image; (**b**,**f**,**h**): diffraction pattern; (**e**,**g**): lattice spacing).

5. Discussion

5.1. Occurrence State of Ti in Groundwater

Ti, as the main element in the Earth's crust, is extensively distributed in rocks and minerals. In most soils and rocks, it is commonly found in the form of octahedral or

tetrahedral coordination within the structure of silicate [26–28]. Additionally, Ti can appear as inclusions of TiO_2 oxides in various minerals [29–31]. Notably, Hu et al. [32] were the first to discover naturally formed TiO_2 nanoparticles, which are widely distributed in a variety of natural media. These nanoparticles can be categorized into three categories: amorphous TiO_2 nanoparticles, crystallographic TiO_2 nanoparticles, and aggregation of TiO_2 nanoparticles.

Through the analysis of nanoparticles in different groundwater layers within the Baotu Spring area, Ti-bearing nanoparticles were identified. These Ti-bearing nanoparticles were found to exist in both crystalline and amorphous forms in the groundwater. The crystalline Ti-bearing nanoparticles exhibited a granular and irregular polymer morphology and were primarily composed of rutile, brookite, anatase, ilmenite, pseudorutile, and ulvospinel. On the other hand, amorphous Ti-bearing nanoparticles showed a granular and irregular polymer morphology, with their main components mainly containing Ti or Ti and Fe. Liang et al. [33] proposed that nanoparticles possess selective adsorption capabilities, particularly for metals, and TiO_2 nanoparticles have demonstrated efficient adsorption of Pb, Cd, Cu, Zn, and Ni [34] during groundwater transport. The Ti-bearing nanoparticles in the study area contained metal elements such as Zn, Ca, Mn, Mo, Cr, and Ni, indicating their potential for effectively transporting metal elements in groundwater. This finding offers a new perspective on the migration of metal elements in groundwater. Moreover, nanoparticles can serve as carriers of inorganic substances, thus enhancing their mobility within the aquatic environment.

5.2. Growth Characteristics of Natural Ti-Bearing Nanoparticles

Through an investigation of the crystallization state of nanoparticles in different groundwater layers, it was found that crystal, amorphous, and Ti-bearing nanoparticles coexisted in the Baotu Spring area. Various growth models have been proposed to explain the crystallization process, including the nucleation and growth model [9,35]. Another mechanism, known as directional attachment, involves the repeated attachment of crystal particles on specific lattice-matched crystal planes [36]. The growth process of crystals may be affected by the surrounding environment [37–39], and their structure is not static but rather undergoes changes in response to the environment [40,41].

By analyzing the characteristics of Ti-bearing nanoparticles in the experimental data, it was observed that these nanoparticles exhibited different growth stages. In Figures 5v and 6a,d, the Ti-bearing nanoparticles were in the initial growth stage, displaying a relatively dispersed distribution without distinct crystal morphology, with some particles aggregated together. In Figures 3a, 5e,p and 7c, the Ti-bearing nanoparticles gather to form overall polymer shapes, while some retain their initial morphology. The SAED patterns also reveal diffraction spots, indicating their crystal morphology. Figures 3d,g,j,m and 4a,d,f show Ti-bearing nanoparticles with regular crystal morphology, aggregating with surrounding nanoparticles, and potentially forming larger polymer morphologies in later stages. Figure 5l displays nanoparticles with regular crystal shapes, with the observation of intersection points in the morphology curves of smaller particles. The aggregation of Ti-bearing nanoparticles has formed an almost perfect crystal shape, as evidenced by the diffraction spots in the SAED patterns. Previous research suggests that amorphous particles gather together during the growth process and undergo recrystallization and conversion to form stable crystal particles at a later stage [37,42,43]. In summary, the transformation process of Ti-bearing nanoparticles from amorphous to crystalline in this study possessed different morphological characteristics. The nanoparticles gradually acquired complete shapes, their degree of crystallization gradually increased, and they tended to aggregate to form crystals. This finding provides insights into the occurrence and growth patterns of natural Ti-bearing nanoparticles and contributes to understanding the geochemical behavior of Ti-bearing nanoparticles in groundwater.

5.3. Environmental Significance of Natural TiO$_2$ Nanoparticles in Karst Groundwater

According to the results of the EDS analysis, Ti-bearing nanoparticles contained other metallic and nonmetallic elements in addition to Ti. Moreover, the elemental composition of Ti-bearing nanoparticles varied among different types of groundwater. Through a comprehensive comparison of the elements contained in Ti-bearing nanoparticles in various groundwater layers, it was observed that central karst water contained a variety of metal and nonmetal elements, possibly affected by the specific aquifer or surrounding rock characteristics. In the case of the Baotu Spring sample, TiO$_2$ nanoparticles were found to consist only of N, O, and Ti, mainly comprising brookite, anatase, and rutile, which are the three naturally occurring isotopic forms of TiO$_2$. Previous studies have demonstrated that TiO$_2$ nanoparticles can facilitate pollutant degradation and removal through the redox reactions induced by ultraviolet light and water [44–46]. Additionally, in industry, nanoscale TiO$_2$ is widely used as an effective adsorbent for arsenic removal in water treatment due to its chemical stability, cost-effectiveness, and environmental safety [47,48]. Hence, it is reasonable to speculate that TiO$_2$ nanoparticles themselves may possess self-purification capabilities. Consequently, the simplified element composition of TiO$_2$ nanoparticles in the Baotu Spring samples may be related to the pollutant removal facilitated by redox reactions in water.

5.4. Hydrogeological Significance of Natural Ti-Bearing Nanoparticles in Karst Groundwater

The sampling sites were divided into the direct discharge area (JS12), the indirect recharge area (LX42, LX44, and YR34), the discharge area (KB5, Baiquan, and Baotu Spring), and the northern geothermal area (Beilin). Currently, several methods are commonly employed to trace and analyze groundwater movement. These methods encompass the utilization of stable isotopes of hydrogen to trace the formation and recharge of groundwater [36,49–51], the adoption of inert chemical components (Cl$^-$ and NO$_3{}^-$) to reflect water–rock interactions in runoff [52–55], and the application of some ion reaction tracers (such as Mg^{2+}, Ca^{2+}, Na$^+$, K$^+$, HCO$_3{}^-$, and SO$_4{}^{2-}$) [56,57].

In this study, Ti-bearing nanoparticles were detected in groundwater samples collected from the direct recharge, indirect recharge, discharge, and northern geothermal areas. Through the analysis of the characteristics of Ti-bearing nanoparticles, variations in the presence of these particles were observed among distinct regions. Notably, brookite was detected in the direct recharge area (JS12), indirect recharge area (LX44), and discharge area (Baiquan and Baotu Spring) (Figure 8). These nanoparticles may indicate the potential use of specific mineral nanoparticles as novel tracers for tracking groundwater migration. Importantly, the utilization of these natural nanoparticles as tracers will have minimal impact on the water environment and pollution levels.
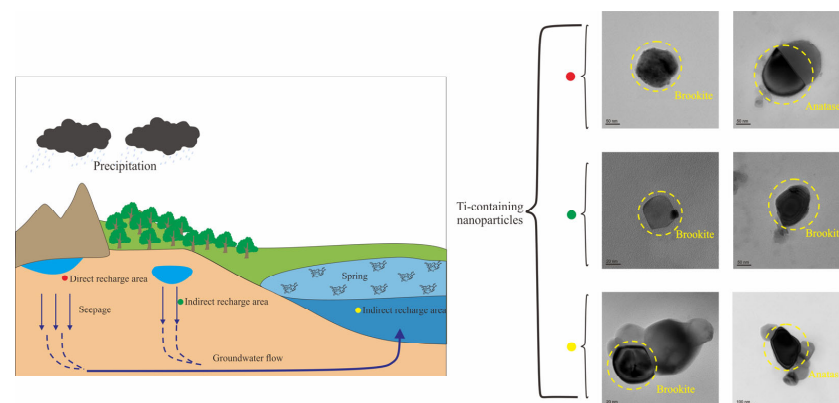

Figure 8. Schematic diagram of the occurrence form of natural Ti-bearing nanoparticles in karst groundwater system.

6. Conclusions

In this study, natural Ti-bearing nanoparticles were observed in various groundwater layers, displaying a granular, irregular polymer morphology indicative of both amorphous and crystalline states. Through an analysis of natural Ti-bearing nanoparticles at various growth stages, it was ascertained that they underwent morphological changes during the transition from an amorphous to a crystalline state. The particles gradually attained a more refined morphology and increased crystallinity, ultimately coalescing to form crystals. This observation contributes to a better understanding of the crystallization process of mineral particles. The identification of natural Ti-bearing nanoparticles in different groundwater layers revealed their compositions, including rutile, brookite, anatase, ilmenite, pseudorutile, and ulvospinel. Additionally, other amorphous nanoparticles mainly contained Ti or a mixture of Ti and Fe. Significantly, the detection of brookite in three distinct regions suggests that natural nanoparticles widely distributed in groundwater systems can serve as mineral tracer particles to track groundwater migration. Moreover, the analysis indicated the presence of additional metal elements in Ti-bearing nanoparticles, such as Zn, Ca, Mn, Mo, Cr, and Ni. This observation demonstrated that Ti-bearing nanoparticles have the capability to transport metal elements in groundwater, providing new insights into the migration behavior of metal elements. Additionally, natural nanoparticles can act as carriers of inorganic substances, thus improving their mobility within the water environment.

References

1. Bakshi, S.; He, Z.L.; Harris, W.G. Natural nanoparticles: Implications for environment and human health. *Crit. Rev. Environ. Sci. Technol.* **2015**, *45*, 861–904. [CrossRef]
2. Frimmel, F.H.; Niessner, R. *Nanoparticles in the Water Cycle: Properties, Analysis and Environmental Relevance*; Springer Science and Business Media LLC.: Dordrecht, The Netherlands, 2010; pp. 1–239. [CrossRef]
3. Wigginton, N.S.; Haus, K.L.; Hochella, M.F. Aquatic environmental nanoparticles. *J. Environ. Monit.* **2007**, *9*, 1306–1316. [CrossRef]
4. Dibyanshu, K.; Chhaya, T.; Raychoudhury, T. A review on the fate and transport behavior of engineered nanoparticles: Possibility of becoming an emerging contaminant in the groundwater. *Int. J. Environ. Sci. Technol.* **2023**, *20*, 4649–4672. [CrossRef]
5. Banfield, J.F.; Zhang, H. Nanoparticles in the environment. *Rev. Miner. Geochem.* **2001**, *44*, 1–58. [CrossRef]
6. Ju, Y.; Li, X.; Ju, L.; Feng, H.; Tan, F.; Cui, Y.; Yang, Y.; Wang, X.; Cao, J.; Qiao, P.; et al. Nanoparticles in the Earth surface systems and their effects on the environment and resource. *Gondwana Res.* **2022**, *110*, 370–392. [CrossRef]
7. Consani, S.; Carbone, C.; Dinelli, E.; Balić-Žunić, T.; Cutroneo, L.; Capello, M.; Salviulo, G.; Lucchetti, G. Metal transport and remobilisation in a basin affected by acid mine drainage: The role of ochreous amorphous precipitates. *Environ. Sci. Pollut. Res.* **2017**, *24*, 15735–15747. [CrossRef] [PubMed]
8. Konrad-Schmolke, M.; Halama, R.; Wirth, R.; Thomen, A.; Klitscher, N.; Morales, L.; Schreiber, A.; Wilke, F.D. Mineral dissolution and reprecipitation mediated by an amorphous phase. *Nat. Commun.* **2018**, *9*, 1637. [CrossRef]
9. Giuffre, A.J.; Hamm, L.M.; Han, N.; De Yoreo, J.J.; Dove, P.M. Polysaccharide chemistry regulates kinetics of calcite nucleation through competition of interfacial energies. *Proc. Natl. Acad. Sci. USA* **2013**, *110*, 9261–9266. [CrossRef]
10. Faulstich, L.; Griffin, S.; Nasim, M.J.; Masood, M.I.; Ali, W.; Alhamound, S.; Omran, Y.; Kim, H.; Kharma, A.; Schäfer, K.H.; et al. Nature's Hat-trick: Can we use sulfur springs as ecological source for materials with agricultural and medical applications? *Int. Biodeterior. Biodegrad.* **2017**, *119*, 678–686. [CrossRef]
11. Nazari, A.; Nakhaei, M.; Yari, A.R. Arsenic Adsorption by TiO_2 Nanoparticles Under Conditions Similar to Groundwater: Batch and Column Studies. *Int. J. Environ. Res.* **2021**, *15*, 79–91. [CrossRef]
12. Eljamal, O.; Sasaki, K.; Tsuruyama, S.; Hirajima, T. Kinetic Model of Arsenic Sorption onto Zero-Valent Iron (ZVI). *Water Qual. Expo. Health* **2011**, *2*, 125–132. [CrossRef]

13. Ken, D.S.; Sinha, A. Recent developments in surface modification of nano zero-valent iron (nZVI): Remediation, toxicity and environmental impacts. *Environ. Nanotechnol. Monit. Manag.* **2020**, *14*, 100344. [CrossRef]

14. Aredes, S.; Klein, B.; Pawlik, M. The removal of arsenic from water using natural iron oxide minerals. *J. Clean. Prod.* **2013**, *60*, 71–76. [CrossRef]

15. Gupta, V.K.; Nayak, A. Cadmium removal and recovery from aqueous solutions by novel adsorbents prepared from orange peel and Fe_2O_3 nanoparticles. *Chem. Eng. J.* **2012**, *180*, 81–90. [CrossRef]

16. Chen, L.; He, B.Y.; He, S.; Wang, T.J.; Su, C.L.; Jin, Y. Fe-Ti oxide nano-adsorbent synthesized by co-precipitation for fluoride removal from drinking water and its adsorption mechanism. *Powder Technol.* **2012**, *227*, 3–8. [CrossRef]

17. Xu, M.; Mao, B.Y.; Zhang, Q. Evolvement and expectation of research on the modern deep karst. *Adv. Earth Sci.* **2008**, *25*, 495–500, (In Chinese with English Abstract).

18. Yue, F.J.; Li, S.L.; Waldron, S.; Wang, Z.J.; Oliver, D.M.; Chen, X.; Liu, C.Q. Rainfall and conduit drainage combine to accelerate nitrate loss from a karst agroecosystem: Insights from stable isotope tracing and high-frequency nitrate sensing. *Water Res.* **2020**, *186*, 116388. [CrossRef] [PubMed]

19. Stevanović, Z. *Karst Aquifers-Characterization and Engineering*; Springer: Berlin/Heidelberg, Germany, 2015.

20. Di, C.B. Study on Comprehensive Technology of Baoquan in Jinan. Master's Thesis, Shandong University, Jinan, China, 2007. (In Chinese with English Abstract)

21. Li, C.M. Analysis on karst resources and preservation of famous springs in Jinan. *Carsologica Sin.* **1985**, *Z1*, 37–745. (In Chinese with English Abstract)

22. Wang, J.Q.; Wu, Y.F.; Qian, J.Z.; Li, F.L. Scheme of groundwater exploited to keep spring spurting and water supply in Jinan Spring zone. *J. Agro-Environ. Sci.* **2004**, *23*, 1228–1231. (In Chinese with English Abstract)

23. Wu, X.P. Experimental Research on Artificial Compensation for Groundwater to Protect Springs in Jinan. Master's Thesis, Wuhan University, Wuhan, China, 2004. (In Chinese with English Abstract)

24. Xu, J.X.; Xing, L.T.; Tong, G.Y.; Fan, L.Q. Groundwater environment evolution and its conservation in Jinan spring catchment. *Hydrogeol. Eng. Geol.* **2004**, *6*, 69–73. (In Chinese with English Abstract)

25. Zou, S.Z.; Zhang, W.H.; Liang, B.; Chen, H.F.; Liang, X.P. A discussion of the assessment of ground water vulnerability in epi karst zone of the karst area, Southwest China. *Earth Sci. Front.* **2005**, *12*, 152–158. (In Chinese with English Abstract)

26. Raman, K.V.; Jackson, M.L. Rutile and anatase determination in soils and sediments. *Am. Mineral. J. Earth Planet. Mater.* **1965**, *50*, 1086–1092.

27. Sayin, M.; Jackson, M.L. Anatase and rutile determination in kaolinite deposits. *Clays Clay Miner.* **1975**, *23*, 437–443. [CrossRef]

28. Baioumy, H.M. Ti-bearing minerals in sedimentary kaolin deposits of Egypt. *Appl. Clay Sci.* **2014**, *101*, 345–353. [CrossRef]

29. Mankin, C.J. Proposed Reference Illite from the Ouachita Mountains of Southeastern Oklahoma1. *Clays Clay Miner.* **1961**, *10*, 372–379. [CrossRef]

30. Weiss, A.; Range, K.J. On titanium in the kaolinite lattice: Int. In Proceedings of the Clay Conference, Jerusalem, Israel, 20–24 June 1966; pp. 53–66.

31. Plavsa, D.; Reddy, S.M.; Agangi, A.; Clark, C.; Kylander-Clark, A.; Tiddy, C.J. Microstructural, trace element and geochronological characterization of TiO_2 polymorphs and implications for mineral exploration. *Chem. Geol.* **2018**, *476*, 130–149. [CrossRef]

32. Hu, G.; Cao, J.; Wang, C.; Lu, M.; Lin, Z.X. Study on the characteristics of naturally formed TiO2 nanoparticles in various surficial media from China. *Chem. Geol.* **2020**, *550*, 119703. [CrossRef]

33. Liang, P.; Shi, T.; Jing, L.I. Nanometer-size titanium dioxide separation/preconcentration and FAAS determination of trace Zn and Cd in water sample. *Int. J. Environ. Anal. Chem.* **2004**, *84*, 315–321. [CrossRef]

34. Engates, K.E.; Shipley, H.J. Adsorption of Pb, Cd, Cu, Zn, and Ni to titanium dioxide nanoparticles: Effect of particle size, solid concentration, and exhaustion. *Environ. Sci. Pollut. Res.* **2011**, *18*, 386–395. [CrossRef]

35. Petsev, D.N.; Chen, K.; Gliko, O.; Vekilov, P.G. Diffusion-limited kinetics of the solution-solid phase transition of molecular substances. *Proc. Natl. Acad. Sci. USA* **2003**, *100*, 792–796. [CrossRef]

36. Penna, D.; Hopp, L.; Scandellari, F.; Allen, S.T.; Benettin, P.; Beyer, M.; Geris, J.; Klaus, J.; Marshall, J.D.; Schwendenmann, L.; et al. Ideas and perspectives: Tracing terrestrial ecosystem water fluxes using hydrogen and oxygen stable isotopes—Challenges and opportunities from an interdisciplinary perspective. *Biogeosciences* **2018**, *15*, 6399–6415. [CrossRef]

37. De Yoreo, J.J.; Gilbert, P.U.P.A.; Sommerdijk, N.A.J.M.; Penn, R.L.; Whitelam, S.; Joester, D.; Zhang, H.; Rimer, J.D.; Navrotsky, A.; Banfield, J.F.; et al. Crystallization by particle attachment in synthetic, biogenic, and geologic environments. *Science* **2015**, *349*, aaa6760. [CrossRef] [PubMed]

38. Lin, D.; Story, S.D.; Walker, S.L.; Huang, Q.; Liang, W.; Cai, P. Role of pH and ionic strength in the aggregation of TiO_2 nanoparticles in the presence of extracellular polymeric substances from Bacillus subtilis. *Environ. Pollut.* **2017**, *228*, 35–42. [CrossRef] [PubMed]

39. Loosli, F.; Le Coustumer, P.; Stoll, S. TiO2 nanoparticles aggregation and disaggregation in presence of alginate and Suwannee River humic acids. pH and concentration effects on nanoparticle stability. *Water Res.* **2013**, *47*, 6052–6063. [CrossRef] [PubMed]

40. Marshall, W.L.; Hall, C.E.; Mesmer, R.E. The system dipotassium hydrogen phosphate-water at high temperatures (100–400 °C); Liquid-liquid immiscibility and concentrated solutions. *J. Inorg. Nucl. Chem.* **1981**, *43*, 449–455. [CrossRef]

41. Zhang, H.; Gilbert, B.; Huang, F.; Banfield, J.F. Water-driven structure transformation in nanoparticles at room temperature. *Nature* **2003**, *424*, 1025–1029. [CrossRef]

42. Guo, H.; Barnard, A.S. Naturally occurring iron oxide nanoparticles: Morphology, surface chemistry and environmental stability. *J. Mater. Chem. A* **2013**, *1*, 27–42. [CrossRef]

43. Zhao, Z.; Tian, J.; Sang, Y.; Cabot, A.; Liu, H. Structure, Synthesis, and Applications of TiO$_2$ Nanobelts. *Adv. Mater.* **2015**, *27*, 2557–2582. [CrossRef]

44. Adesina, A.A. Industrial exploitation of photocatalysis: Progress, perspectives and prospects. *Catal. Surv. Asia* **2004**, *8*, 265–273. [CrossRef]

45. Chitose, N.; Ueta, S.; Seino, S.; Yamamoto, T.A. Radiolysis of aqueous phenol solutions with nanoparticles. 1. Phenol degradation and TOC removal in solutions containing TiO$_2$ induced by UV, γ-ray and electron beams. *Chemosphere* **2003**, *50*, 1007–1013. [CrossRef]

46. Kabra, K.; Chaudhary, R.; Sawhney, R.L. Treatment of hazardous organic and inorganic compounds through aqueous-phase photocatalysis: A review. *Ind. Eng. Chem. Res.* **2004**, *43*, 7683–7696. [CrossRef]

47. Carp, O.; Huisman, C.L.; Reller, A. Photoinduced reactivity of titanium dioxide. *Prog. Solid State Chem.* **2004**, *32*, 33–177. [CrossRef]

48. Ma, L.; Tu, S. Arsenic removal from water using a modified rutile ore and the preliminary mechanisms. *Desalination Water Treat.* **2011**, *32*, 445–452. [CrossRef]

49. Kabra Clark, I.D.; Fritz, P. *Environmental Isotopes in Hydrogeology*; CRC Press: Boca Raton, FL, USA, 1997.

50. Jasechko, S. Global Isotope Hydrogeology—Review. *Rev. Geophys.* **2019**, *57*, 835–965. [CrossRef]

51. Sappa, G.; Barbieri, M.; Ergul, S.; Ferranti, F. Hydrogeological Conceptual Model of Groundwater from Carbonate Aquifers Using Environmental Isotopes (18O, 2H) and Chemical Tracers: A Case Study in Southern Latium Region, Central Italy. *J. Water Resour. Prot.* **2012**, *4*, 695–716. [CrossRef]

52. Edmunds, W.M. Groundwater nitrate as a palaeoenvironmental indicator. In *Geochemistry of the Earth's Surface*; Springer: Berlin/Heidelberg, Germany, 1999; pp. 35–39.

53. Edmunds, W.M.; Smedley, P.L. Residence time indicators in groundwater: The East Midlands Triassic sandstone aquifer. *Appl. Geochem.* **2000**, *15*, 737–752. [CrossRef]

54. Glynn, P.D.; Plummer, L.N. Geochemistry and the understanding of ground-water systems. *Hydrogeol. J.* **2005**, *13*, 263–287. [CrossRef]

55. Han, D.; Kohfahl, C.; Song, X.; Xiao, G.; Yang, J. Geochemical and isotopic evidence for palaeo-seawater intrusion into the south coast aquifer of Laizhou Bay, China. *Appl. Geochem.* **2011**, *26*, 863–883. [CrossRef]

56. Stimson, J.; Frape, S.; Drimmie, R.; Rudolph, D. Isotopic and geochemical evidence of regional-scale anisotropy and interconnectivity of an alluvial fan system, Cochabamba Valley, Bolivia. *Appl. Geochem.* **2001**, *16*, 1097–1114. [CrossRef]

57. Pan, G.F.; Li, X.Q.; Zhang, J.; Liu, Y.D.; Liang, H. Groundwater-flow-system characterization with hydrogeochemistry: A case in the lakes discharge area of the Ordos Plateau, China. *Hydrogeol. J.* **2019**, *27*, 669–683. [CrossRef]